Article:
Alsebaie, D.M. and Morley, N.A. (2026) Improved mechanical performance of FeCoNiAlMn films through controlled annealing. Journal of Materials Research and Technology, 43. pp. 1618-1627. ISSN: 2238-7854

https://doi.org/10.1016/j.jmrt.2026.06.180

Improved Mechanical Performance of FeCoNiAlMn films through Controlled Annealing

D.M. Alsebaie [1,2,*] and N. A. Morley [2]

[1] Physics Department, King Abdulaziz University, Jeddah, Saudi Arabia

[2] School of Chemical, Materials and Biological Engineering, University of Sheffield, S1 3JD, UK

[*] Corresponding author: Dalsebaie1@sheffield.ac.uk

Key words: sputtering, FeCoNi, nanoindentation, hardness, mechanical properties.

Abstract

As soft magnetic materials continue to attract significant attention, investigating their mechanical properties has become increasingly important. In this study, FeCoNiAlMn alloys with varying elemental concentrations and annealing temperatures were examined to evaluate their mechanical behaviour. Alloys were fabricated using DC magnetron sputtering using three separate targets: FeCoNi, Al, and Mn under an argon atmosphere. All films had an approximate thickness of 600 nm. The alloys were investigated in the as-deposited state and after annealing at 400 °C, 600 °C, and 800 °C for one hour. X-ray Photoelectron Spectroscopy (XPS) was employed to determine the elemental composition of each alloy, while X-ray Diffraction (XRD) analysis revealed variations in crystal structure associated with changes in elemental ratios and heat treatment conditions. The mechanical properties were evaluated using a nanoindenter. The $FeCoNi_{0.8}$ alloy exhibited a significant improvement in hardness with increasing annealing temperature, reaching approximately 16 GPa when annealed 600 °C, about three times higher than its as-deposited value. In contrast, the $Fe_{1.1}CoNiAl_{1.5}Mn_{5.4}$ alloy showed a considerable reduction in hardness, decreasing from around 5 GPa for the as-deposited film to approximately 0.9 GPa after annealing at 600 °C.

Introduction

High-entropy alloys (HEAs) represent a novel strategy in metallic materials design. Since the pioneering works of Yeh and Cantor, who first articulated the principles of high-entropy and multi-component alloy systems, these materials have attracted significant scientific attention due to their exceptional structural and functional characteristics [1, 2]. With carefully engineered compositions, the HEAs can exhibit outstanding performance across multiple domains, including high strength [3], superior ductility [4], and remarkable resistance to oxidation and irradiation [5]. Additionally, this versatility means that HEAs have exceptional potential for diverse applications, particularly in areas requiring superior mechanical performance [6, 7], corrosion resistance [8, 9], and high-temperature (refractory) stability [10]. Most HEA systems are predominantly composed of transition metals such as Co, Ni, Fe, Mn, and Cr, and are further tailored with additional elements, including Al, Cu, V, Ti, and Mo, to enhance their structural and functional properties [1, 11-14]. In particular, the FeCoNiMnAl alloy system has recently gained attention as a promising candidate for structural and/or magnetic applications owing to its cost efficiency, excellent corrosion resistance, favourable magnetic characteristics, and, most importantly, its tuneable mechanical properties achievable through microstructural optimisation [15, 16].

Nevertheless, the limited mechanical strength of face-centred cubic (FCC) structured alloys remains a major drawback, constraining their practical applicability. The mechanical behaviour of metallic materials can generally be improved through mechanisms such as grain refinement, precipitation strengthening, solid-solution hardening, and the generation of high dislocation densities[17, 18]. Numerous investigations have shown that oxide dispersion strengthening (ODS) offers an efficient approach to improving the mechanical performance of alloys by refining the grain structure and restricting dislocation mobility.[19]. Hadraba et al. [20] reported that the addition of 0.3 wt.% oxide particles to CoCrFeNiMn resulted in a 50% reduction in grain size (from 0.8 μm to 0.4 μm). Consequently, the yield strength and ultimate tensile strength increased by approximately 30% at room temperature (from 971 to 1269 MPa and from 1010 to 1318 MPa, respectively), while at 800 °C they increased by about 75% and 68% (from 31.5 to 55 MPa and from 40.5 to 68 MPa, respectively). Du et al. [21] reported that the room-temperature mechanical properties of $(CoCrFeNi)_{100-x}Gd_x$ HEAs were significantly enhanced through several strengthening mechanisms, including grain refinement, solid-solution strengthening, and second-phase strengthening. Among these, grain refinement was identified as the dominant factor, while the alloy still retained good plasticity. In particular, the Gd3-alloy achieved a yield strength of up to 650 MPa, which is nearly three times higher than that of the CoCrFeNi HEA (235 MPa), while maintaining a fracture strain of 36.4%. Tekin et al. [22] reported that when high-energy mechanical alloying was employed to synthesize Y-additions to (1 and 4 at.%) CoCrFeNi HEAs, the resulting hardness increased progressively from 3.45 GPa for the base HEA to 4.18 GPa for the 1Y-alloy and 4.38 GPa for the 4Y-alloy, thus confirming the strengthening effect of Y addition. Also, Tekin et al. [23] reported that Y_2O_3-reinforced CoCrFeNi multicomponent HEA exhibited a marked hardness increase, from 371 ± 13 $HV_{0.5}$ in the unreinforced alloy to 592 ± 20 $HV_{0.5}$ and 685 ± 30

$HV_{0.5}$ with 1 wt.% and 4 wt.% Y_2O_3 additions, respectively. Le Minh Duc et al. [16] report that a single-phase FCC structure was observed in the as-cast condition of $FeCoNiAl_{0.25}Mn_{0.75}$. During annealing at 700 and 800°C, a fine needle-shaped body-centred cubic (BCC) phase precipitated within the FCC matrix, resulting in a pronounced improvement in mechanical performance. Specifically, heat treatment at 700 °C for 24 h increased the hardness from 1.34 GPa to 1.90 GPa, while the yield strength and ultimate tensile strength increased by 64% and 61%, respectively. Also, when the $Al_{0.5}CoCrFeNi$ alloy was processed at elevated temperatures, this induces a gradual transformation from a stable FCC structure to a BCC structure, thereby resulting in an increase in hardness [24].

Although related FeCoNi-based alloy systems have been previously reported, limited studies have addressed the effect of heat treatment on their mechanical properties, particularly in thin-film form. In the present work, FeCoNi and FeCoNiAlMn films with different elemental compositions and annealing temperatures were systematically investigated to clarify the combined influence of alloying and annealing on their structural evolution and mechanical response

The selected annealing temperatures were guided by previous studies on related alloy systems [25-27], in which similar temperature ranges were used to investigate annealing-induced property changes and yielded promising results. In the present study, the same temperature range was adopted to assess its influence on the structural and mechanical behaviour of the films. The annealing duration of 1 h was selected considering the thin-film nature of the samples, where shorter diffusion distances and faster structural response can make shorter annealing times sufficient to induce measurable changes.

Experimental Procures

In this work, three series of alloys were fabricated at room temperature using a direct current (DC) magnetron sputtering system equipped with three separate targets: FeCoNi, Al, and Mn. The alloys were grown on oxidized silicon substrates with a (100) crystallographic orientation, each cut to dimensions of 1 cm × 1 cm. Before deposition, the substrates were ultrasonically cleaned in acetone and isopropanol for approximately 10 minutes and subsequently dried under nitrogen gas. The sputter chamber was evacuated to a base pressure in the low 10^{-7} Torr range before deposition, and the working Ar pressure during sputtering was maintained at 5×10^{-3} Torr.

Three sputtering targets were utilised: a ternary FeCoNi alloy containing equal atomic ratios of Fe, Co, and Ni (33.3% each), high-purity aluminium (99.999%), and manganese with 99.9% purity. The first composition was only the FeCoNi target operating at 70 W. For the second and third compositions, the FeCoNi target was sputtered at 70 W together with the Al target at 30 W, while the Mn target was sputtered at 70 W for the second composition and at 105 W for the third

composition. All alloys were deposited to a total thickness of approximately 600 nm. From each composition, four samples were prepared; one was kept as-deposited while the remaining three were annealed at 400 °C, 600 °C, and 800 °C, respectively, for one hour. The annealing process was performed under flowing Ar gas with a heating rate of 2 °C/min and followed by natural slow cooling inside the furnace.

The structural properties of the thin films were examined using X-ray diffraction (XRD). Measurements were conducted on a Bruker D2 Phaser diffractometer equipped with a Cu $K\alpha_1$ radiation source ($\lambda = 1.54184$ Å) operating at 40 kV and 40 mA. Conventional θ–2θ geometry was employed, and diffraction scans were collected over the 25°–65° range with a step size of 0.020°, enabling analysis of the film structure while avoiding the intense Si substrate peak near 69°. To evaluate the chemical composition, X-ray photoelectron spectroscopy (XPS) analyses were carried out using a Kratos Supra instrument with a monochromated Al Kα source (photon energy 1486.6 eV). Two analysis locations were selected on each film within a 700 μm × 300 μm area. Survey spectra were recorded between 0 and 1200 eV at a pass energy of 160 eV and a step size of 1 eV, with each scan acquired in a single 300-s sweep. Mechanical characterisation was performed using nanoindentation. A standard Berkovich diamond indenter (142°) was employed, with a tip Poisson's ratio of 0.07 and a tip modulus of 1.14×10^3 N mm^{-2}. Each sample was tested with a 10 × 10 indentation matrix (100 indents total) spaced 5 μm apart, and the target indentation depth was approximately 50 nm.

XPS and XRD Results

Figure 1(a) presents the X-ray photoelectron spectroscopy (XPS) spectra of Mn for the as-deposited alloys, illustrating an increase in peak intensity with increasing Mn content in the respective compositions. This trend is consistent with the increase in the Mn target power used during sputtering. From the XPS spectra, the elemental compositions of each alloy were quantified using CasaXPS software and are listed in table 1.

Table 1. Elemental Composition of the alloys determined by XPS

Alloy	Co (at %)(±4)	Fe (at %)(±4)	Ni (at %)(±4)	Mn (at %)(±4)	Al (at %)(±4)
$FeCoNi_{0.8}$	35.5	35.9	28.6	0	0
$Fe_{1.3}CoNiAl_{1.5}Mn_{2.5}$	13.5	17.6	13.9	34.5	20.5
$Fe_{1.1}CoNiAl_{1.5}Mn_{5.4}$	10	10.9	10.1	54	15

Using these compositions, the thermodynamic prediction equations [28] can be used to predict the phases present in the films and whether the films will be solid-solutions. The average valence electron concentration (VEC) provides a prediction as to whether the alloys will be FCC (VEC > 8) or BCC (VEC < 6.87) or both FCC and BCC (8 > VEC > 6.87). For these FeCoNiMnAl films, it is predicted that the $FeCoNi_{0.8}$ film will be FCC (VEC = 8.9), while both the $Fe_{1.3}CoNiAl_{1.5}Mn_{2.5}$ and $Fe_{1.1}CoNiAl_{1.5}Mn_{5.4}$ films having VEC ~ 7, which means they are predicted to contain both BCC and FCC phases. This is due to the Al (VEC = 3) and Mn (VEC = 7) additions having smaller VECs compared to Fe, Ni and Co. Another thermodynamic parameter used to predict solid-solutions is the average enthalpy of mixing, ΔH, which if it is between -22 kJ/mol and 7.5 kJ/mol, the alloy is predicted to be a solid-solution. The $FeCoNi_{0.8}$ film ΔH is -1.33 kJ/mol, while the two films with the addition of Mn and Al: $Fe_{1.3}CoNiAl_{1.5}Mn_{2.5}$ film ΔH = -14.3 kJ/mol and $Fe_{1.1}CoNiAl_{1.5}Mn_{5.4}$ film ΔH = -12.3 kJ/mol. Thus all three films should be solid-solutions, with no intermetallics present.

Figure 1(b) shows the XRD spectra of the $FeCoNi_{0.8}$ films. For the as-deposited film, a single diffraction peak characteristic of the FCC structure appears at approximately 44° [14, 29]. After annealing at 400 °C and 600 °C, this peak shifts due to the thermal treatment. At 400 °C, the diffraction peak shifts slightly to higher angles, indicating a reduction in the interplanar spacing d, as described by Bragg's law ($2d\sin\theta = n\lambda$). This behaviour can be attributed to lattice contraction resulting from stress relaxation and local atomic rearrangement within the metallic FCC structure. In contrast, at 600 °C, the peak moves to a lower angle, corresponding to a decrease in θ and consequently an increase in d-spacing. This expansion is consistent with the appearance of additional FCC-type oxide reflections (FeCo-rich oxide and FeSi-rich oxide) [29] (PDF No. 04-026- 0037), as FCC oxides generally possess slightly larger lattice spacings compared with the metallic FCC phase. Although the difference could also be due to element separation between the FCC-oxide phase and the metallic FCC phase, where the FCC-oxide is say Fe rich and the metallic

FCC phase is say Ni or Co rich. Figure 1(c) presents the XRD patterns of the $Fe_{1.3}CoNiAl_{1.5}Mn_{2.5}$ alloy at different annealing temperatures. The as-deposited film exhibits body-centred cubic (BCC) reflection, which is expected due to the incorporation of Al and Mn into the FeCoNi and is also predicted to form from the average VEC calculations [30]. Upon annealing to 400 °C, the alloy retains its BCC structure. However, at 600 °C, the alloy evolves into a multi-phase structure. The BCC peak is still present; while additional peaks corresponding to FCC-type oxides emerge along with peaks associated with the trigonal phase of Fe_2O_3 (R). This demonstrates that oxidation becomes more significant at this temperature, driven by enhanced atomic mobility that allows oxygen incorporation into the lattice. At the highest annealing temperature of 800 °C, the BCC peak completely disappears. The diffraction pattern becomes dominated by FCC oxide peaks together with FCC metallic reflections. Figure 1(d) illustrates the XRD patterns of the $Fe_{1.1}CoNiAl_{1.5}Mn_{5.4}$ alloy. In the as-deposited state, the alloy exhibits a weak and broad FCC diffraction peak, which is most likely attributed to the high Mn content. After annealing at 400 °C, a pronounced BCC peak emerges alongside a FCC oxide peak, clearly demonstrating the influence of thermal treatment on phase formation and crystallisation. Upon annealing at 600 °C, the BCC peak shifts toward a higher diffraction angle while its intensity decreases. This shift corresponds to a reduction in the interplanar spacing and suggests lattice contraction due to further atomic rearrangement. Moreover, the diffraction pattern reveals the presence of FCC metallic and FCC oxide peaks, accompanied by the trigonal Fe_2O_3 phase (R). After annealing at 800 °C, the BCC peak disappears, and only an FCC metal and oxide peak remains. This behaviour is similar to that observed for the previous alloy at 800 °C and indicates that the BCC phase is no longer stable at such high annealing temperatures. Previous work on HEAs, have shown that Fe will phase separate after annealing from Ni, Mn and Al [31, 32], the appearance of a FCC oxide with lattice constants similar to Fe_3O_4 and a metallic FCC phase with lattice constant similar to FCC phases measured in FeCoMnAl alloys, suggests this may have happen within these films.

Athough annealing was carried out under Ar atmosphere, the presence of FCC oxide reflections suggests that limited oxidation still occurred, most likely due to trace residual oxygen in the annealing chamber, incomplete removal of atmospheric gases, or oxygen exposure of the film surface during cooling or post-annealing handling. Figure 2 shows a schematic representation of the phase transformations induced by heat treatment, providing a visual guide for the structural analysis in Figure 1 (b), (c), and (d). Table 2 provides an overview of the lattice constants and grain size for each of the films, determined from the XRD. It is observed that the results indicate that both the crystal structure and microstructure of the films are strongly affected by annealing. The lattice parameter also changes with phase type, with much larger values recorded for the oxide-related phases than for the metallic FCC and BCC phases. Additionally, the grain size shows a noticeable increase after annealing at higher temperatures, indicating grain growth and microstructural coarsening, especially in the oxide phases, where larger crystallite sizes are recorded compared to the as-deposited state.

Table 2. Lattice constants and grain sizes of FeCoNiAlMn films obtained from XRD patterns at different annealing temperatures (RT, 400°C, 600°C, and 800°C). The lattice parameters were calculated using the cubic lattice-spacing formula, and the grain sizes were estimated using the Scherrer equation.

samples	Annealing	2 θ	Miller Indices	Lattice parameter (Å)	Grain Size D (Å)
$FeCoNi_{0.8}$	RT	44.06	FCC (111)	3.55	102
	400	44.43	FCC (111)	3.52	78
	600	43.36	FCC (111)	3.61	178
		35.71	FCC Oxide (311)	8.33	173
		36.62	FCC oxide (222)	8.5	134
		37.27	FCC oxide (222)	8.3	279
		62.97	FCC Oxide (440)	8.34	150
$Fe_{1.3}CoNiAl_{1.5}Mn_{2.5}$	RT	44.36	BCC (110)	2.88	74
	400	43.93	BCC (110)	2.91	60
	600	44.91	BCC (110)	2.85	91
		29.06	FCC Oxide (220)	8.68	241
		32.74	R (104)	11.27	318
		60.21	FCC oxide (511)	8	176
	800	43.29	FCC (111)	3.62	237
		30.05	FCC Oxide (220)	8.40	228
		35.5	FCC Oxide (311)	8.38	173
		62.74	FCC Oxide (440)	8.37	132
$Fe_{1.1}CoNiAl_{1.5}Mn_{5.4}$	RT	43.42	FCC (111)	3.6	66
	400	44.21	BCC (110)	2.89	142
		35.57	FCC Oxide (311)	8.36	173
	600	44.91	BCC (110)	2.85	153
		28.97	FCC Oxide (220)	8.71	256
		32.42	R (104)	11.38	258
		60.06	FCC oxide (511)	8	170
	800	43.35	FCC (111)	3.61	194
		29.25	FCC Oxide (220)	8.63	684
		32.94	R (104)	11.20	276
		35.6	FCC Oxide (311)	8.36	174
		36.3	FCC oxide (222)	8.6	279
		60.6	FCC oxide (511)	8	354

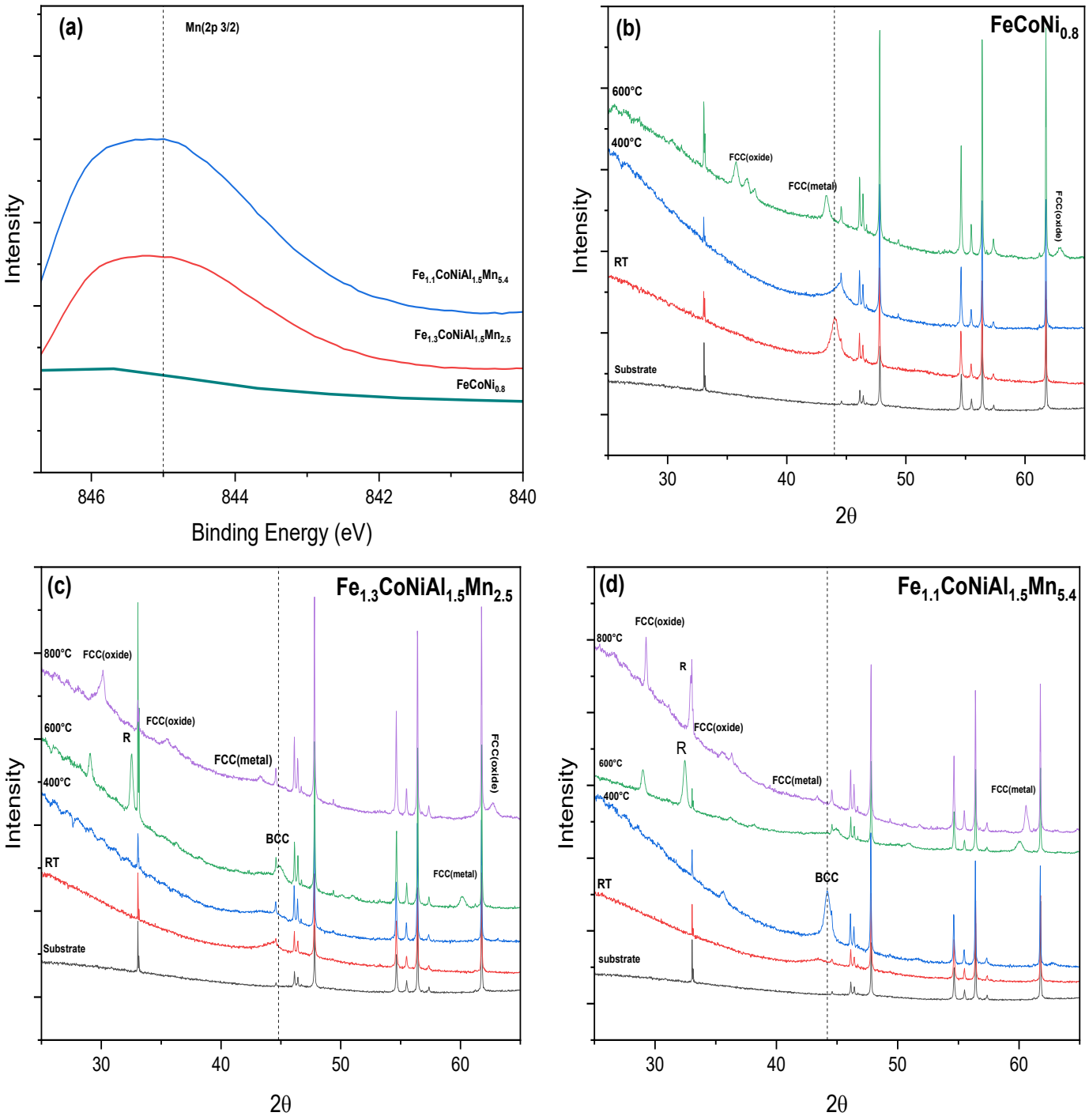

Figure 1. (a) XPS spectra corresponding to the Mn (2p 1/2) for $FeCoNi_{0.8}$, $Fe_{1.3}CoNiAl_{1.5}Mn_{2.5}$, and $Fe_{1.1}CoNiAl_{1.5}Mn_{5.4}$. (b), (c), and (d) X-ray diffraction (XRD) measurements for $FeCoNi_{0.8}$, $Fe_{1.3}CoNiAl_{1.5}Mn_{2.5}$, and $Fe_{1.1}CoNiAl_{1.5}Mn_{5.4}$ alloys, respectively, at different annealing temperatures.

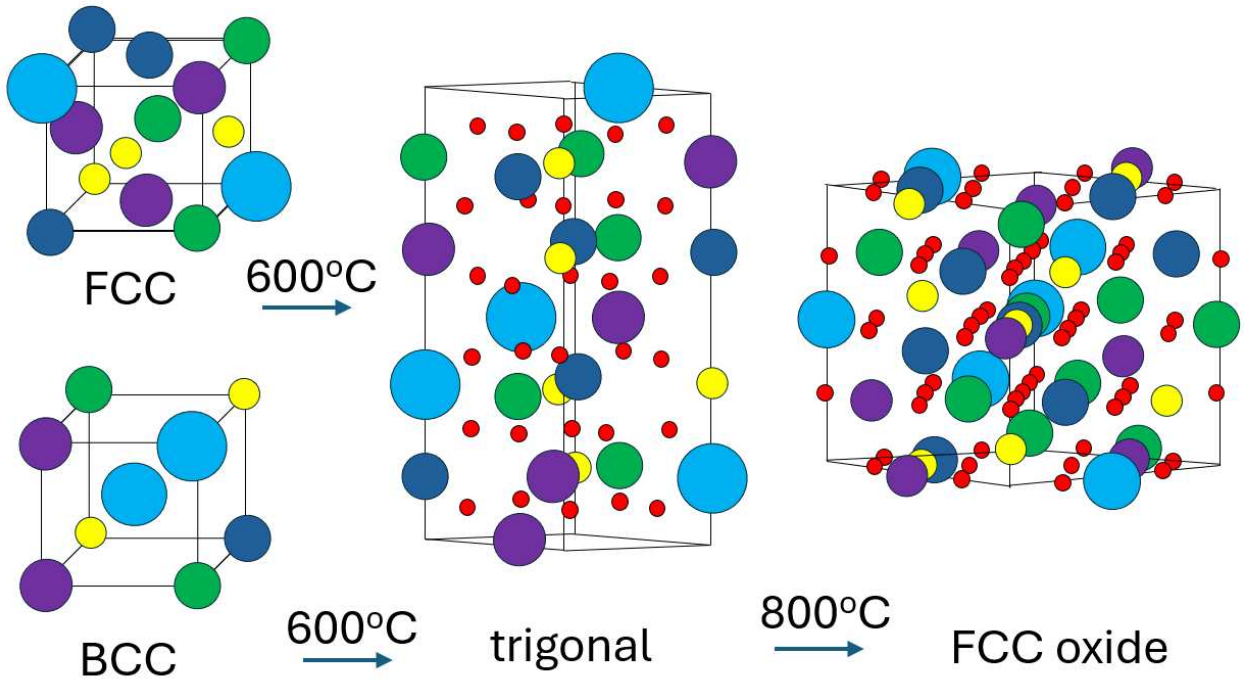

Figure 2. shows the structural evolution of the films during annealing. The coloured atoms represent the metallic elements (Co, Fe, Ni, Mn, and Al), while the red atoms represent oxygen ions.

Mechanical properties

Figure 3 (a) shows the load–displacement curves of the $FeCoNi_{0.8}$ alloy at different annealing temperatures. The as-deposited and 400 °C-annealed samples exhibit comparable behaviour, indicating similar mechanical responses. In contrast, the film annealed at 600 °C requires a higher load to achieve a 50 nm indentation depth, suggesting structural modifications during annealing enhanced the hardness and resistance to deformation. However, it appears that increasing the annealing temperature does not affect all composites equally, as shown in figures 3(b) and (c). Those samples with a higher Mn content exhibit a different response, which can be attributed to the presence of Mn, a brittle element known to reduce ductility [33], as well as to the changes in phase constitution and annealing-induced microstructural evolution associated with the emergence of a multiphase structure . We can extract from figures 3 (a), (b), and (c) the ratio between the final indentation depth (h_f) and the maximum indentation depth under peak load (h_{max}). This ratio is bounded between 0 and 1 ($0 \leq h_f / h_{max} \leq 1$) and serves as an indicator of the material's deformation behaviour, i.e. whether it is predominantly elastic or plastic. A value of $h_f / h_{max} = 0$ corresponds to completely elastic recovery, whereas $h_f / h_{max} = 1$ indicates fully plastic deformation [34]. Figure 3(d) presents this factor and shows a general decrease as the annealing temperature increases, which is consistent with the observed increase in hardness and indicates improved resistance to plastic deformation with heat treatment**.** However, the $Fe_{1.1}CoNiAl_{1.5}Mn_{5.4}$ composition, which contains the highest Mn content, exhibits a consistently higher h_f / h_{max} ratio at all annealing temperatures compared with the other composites, which indicates that this alloy undergoes predominantly plastic deformation.

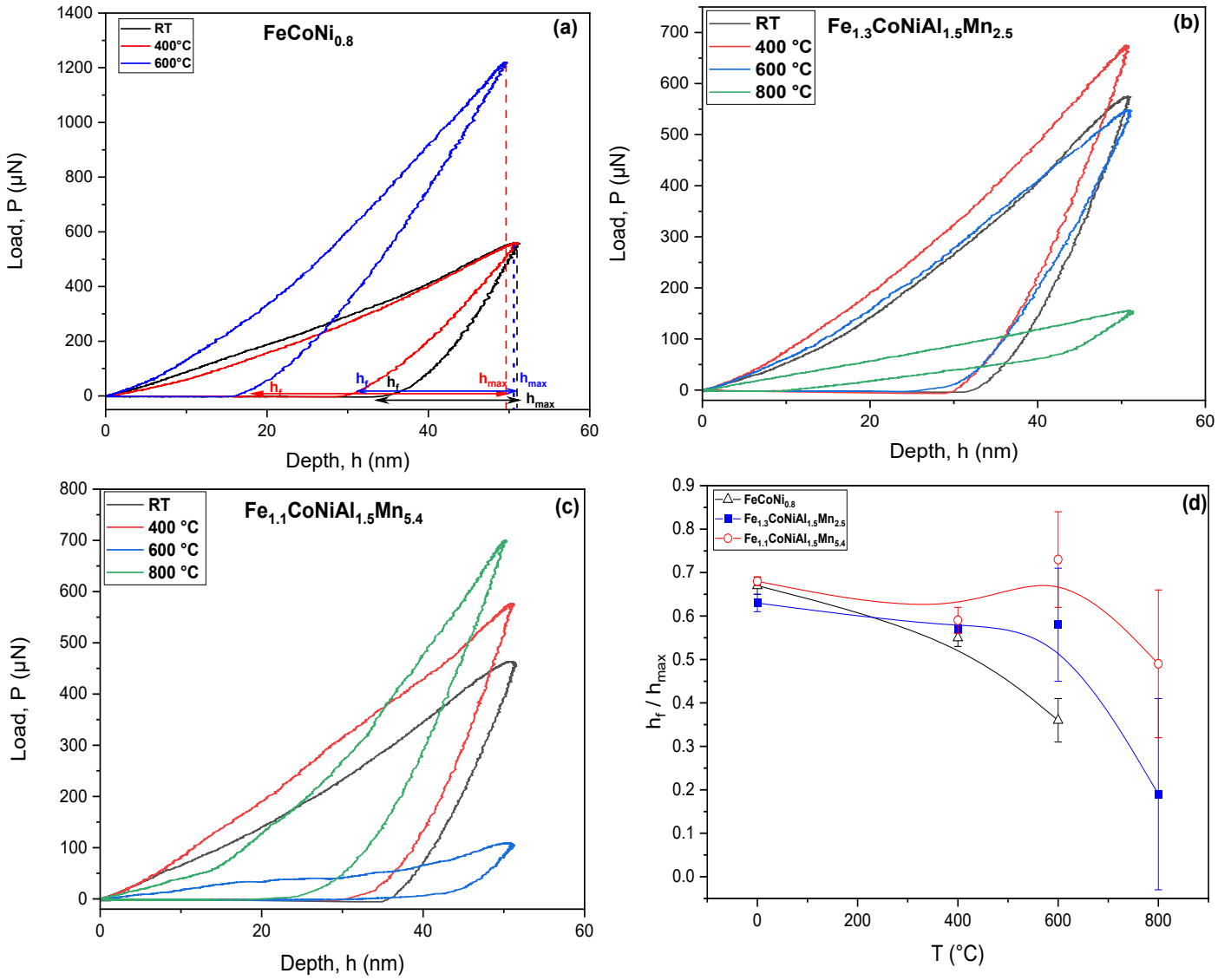

Figure 3. Comparison of load–depth curves for $FeCoNi_{0.8}$, $Fe_{1.3}CoNiAl_{1.5}Mn_{2.5}$, and $Fe_{1.1}CoNiAl_{1.5}Mn_{5.4}$ alloys (600 nm) at different annealing temperatures: room temperature (RT), 400 °C, 600 °C, and 800 °C. The curves also indicate the maximum indentation depth (h_{max}) and the final depth (h_f) during unloading. (d) The ratio of h_f/h_{max} for $FeCoNi_{0.8}$, $Fe_{1.3}CoNiAl_{1.5}Mn_{2.5}$, and $Fe_{1.1}CoNiAl_{1.5}Mn_{5.4}$ alloys as a function of annealing temperature. The lines are a guide for the eye.

The data presented in Figure 3, was also fitted by Oliver and Pharr Method [35, 36], followed by extracting the hardness, H, and reduced modulus of elasticity, E_r. Both properties are derived from the equations below [37, 38]

$$H = \frac{P_{max}}{A_c} \quad (1)$$

$$E_r = \frac{\sqrt{\pi}}{2}\beta\frac{S}{\sqrt{A_c}} \quad (2)$$

where P_{max}represents the maximum applied load, A_c denotes the projected contact area of the indentation, β is a correction factor, and S represents the contact stiffness.

The determination of E_r allows the estimation of the Young's modulus (E_s) of the sample under test, which is expressed as [37]:

$$\frac{1}{E_r} = \frac{1-v_s^2}{E_s} + \frac{1-v_i^2}{E_i} \quad (3)$$

Where v_s is the Poisson's ratio of the film, E_s is the Young's modulus of the film, v_i is the Poisson's ratio of the indenter (0.07), and E_i is the Young's modulus of the indenter (1140 GPa).

Figure 4 shows that the as-deposited $FeCoNi_{0.8}$ alloy exhibits a hardness of approximately 6.5 GPa. This value increases by about 10% upon annealing at 400 °C. However, after annealing at 600 °C, the hardness shows a significant rise, reaching more than double its initial value, approximately 16 GPa. This behaviour is evident in Figure 3 (a), where a pronounced change appears in the load-displacement curve. For previous hardness measurements on thin films, Baco et al. [37] found that for 600 nm polycrystalline FeCo films, the hardness was 14.8 nm, while Abbas et al. [34] reported hardness values of about 6 GPa for amorphous FeSiB thin films with a thickness of 668 nm and about 5 GPa for amorphous FeGaSiB thin films with a thickness of 640 nm. Therefore, the present polycrystalline $FeCoNi_{0.8}$ film annealed at 600 °C exhibits competitive mechanical performance.

The modest increase in hardness after annealing at 400 °C can be correlated with the structural refinement of the metallic phase, as evidenced by the decrease in grain size and the slight reduction in lattice parameter, as shown in table 2. At 600 °C, however, the XRD pattern changes markedly, with the appearance of multiple diffraction peaks that indicate substantial phase evolution and the formation of oxide-related phases. Therefore, the larger increase in hardness at 600 °C is likely governed not only by refinement effects but also by multiphase and oxide-assisted strengthening mechanisms. Moreover, the reduced modulus and Young's modulus follow a different trend. Both attain their highest values in the as-deposited film, decrease by ~30% after annealing at 400 °C, and recover at 600 °C to levels comparable to the as-deposited state. This non-monotonic behaviour is likely related to annealing-induced structural changes. In particular, the 400 °C sample shows a slight reduction in lattice parameter together with a decrease in grain size, indicating modification of the FCC metallic phase. In contrast, the 600 °C sample exhibits multiple

diffraction peaks, suggesting significant phase evolution and the development of a more complex structure, which may contribute to restoring the elastic response.

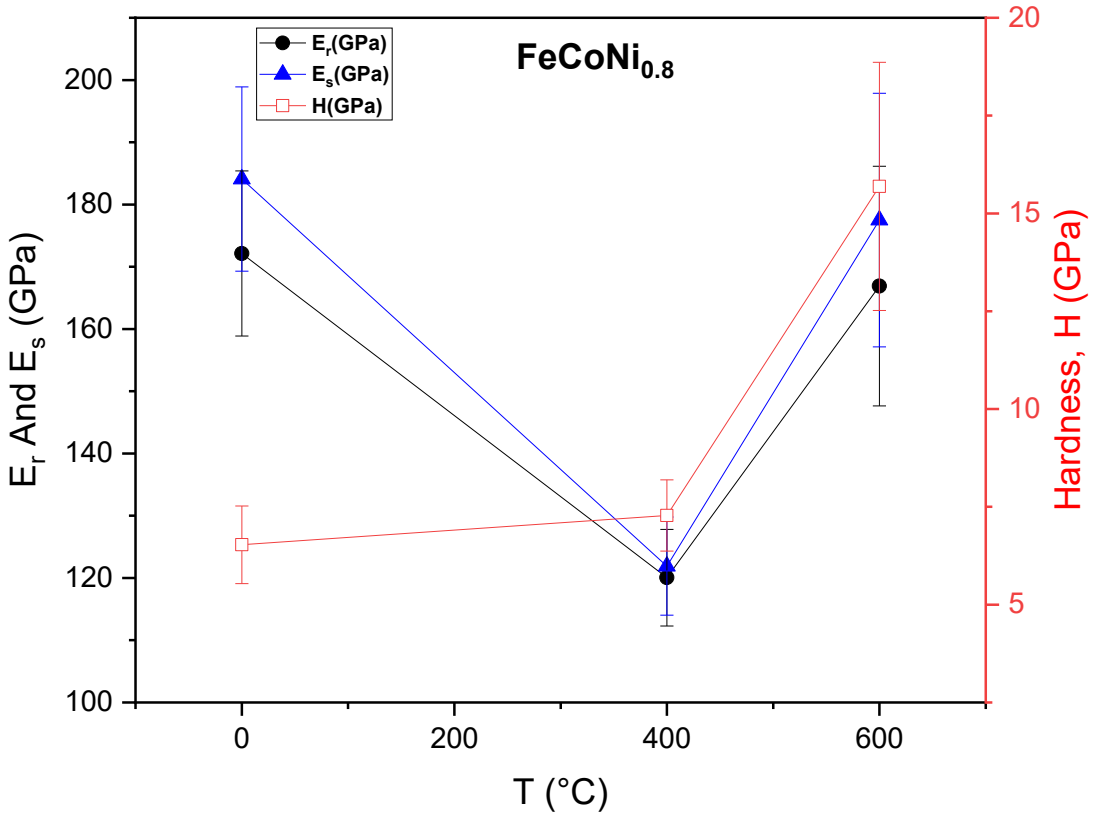

Figure 4. Comparison of hardness (H), Young's modulus (E_s), and reduced modulus (E_r) of $FeCoNi_{0.8}$ thin films at different annealing temperatures. The lines are a guide for the eye.

Figure 5 shows the variation in hardness of the $Fe_{1.3}CoNiAl_{1.5}Mn_{2.5}$ alloy at different annealing temperatures. At room temperature, the hardness is approximately 5.7 GPa, which is about 15% (1 GPa) lower than that of $FeCoNi_{0.8}$. This decrease is most likely attributed to the addition of Al and Mn, as Mn is relatively brittle element that tend to reduce the overall hardness of the alloy [33] , and the lower hardness is also could influenced by the resulting changes in phase constitution and annealing-induced microstructural evolution associated with the emergence of a multiphase structure. Upon annealing at 400 °C, the hardness increases by nearly 50%, possibly due to crystal structure reordering and the relaxation of internal stresses. However, at 600 °C, the hardness

decreases from 8.4 GPa to 4.8 GPa, likely because of the formation of a multi-phase structure composed of both BCC and FCC phases. At 800 °C, the measured hardness drops further to around 3 GPa, most likely because the surface has become non-uniform, as indicated by the large experimental error. This non-uniformity may arise from grain coarsening, surface oxidation, and elemental segregation. The reduced modulus and Young's modulus follow a similar trend to that of the hardness, suggesting that they share the same underlying interpretation.

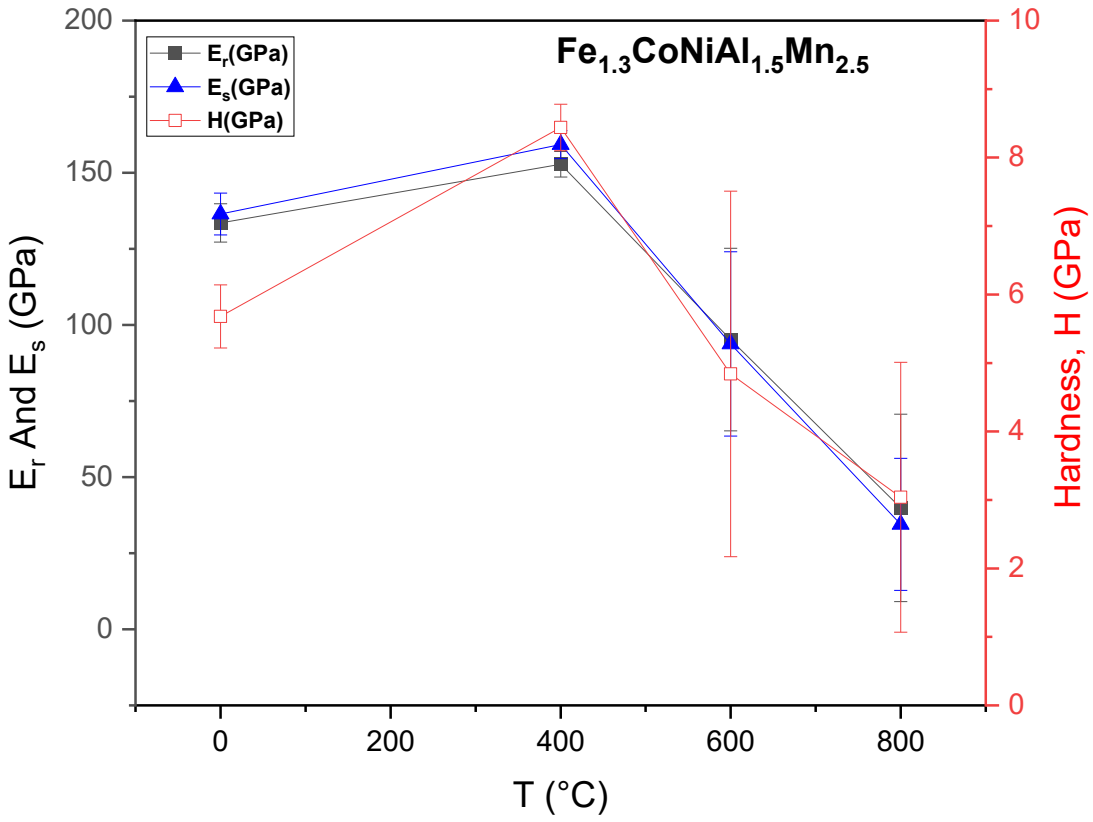

Figure 5. Comparison of hardness (H), Young's modulus (E_s), and reduced modulus (E_r) of $Fe_{1.3}CoNiAl_{1.5}Mn_{2.5}$ alloy at different annealing temperatures. The lines are a guide for the eye.

Figure 6 gives the hardness, reduced modulus, and Young's modulus of the $Fe_{1.1}CoNiAl_{1.5}Mn_{5.4}$ alloy. The hardness of the as-deposited remains lower than that of the $FeCoNi_{0.8}$ and $Fe_{1.3}CoNiAl_{1.5}Mn_{2.5}$ as-deposited alloys. This reduction is mainly attributed to the higher Mn content in the alloy. Moreover, Mn may influence phase stability and alter the stacking fault energy in HEAs, thereby affecting the active deformation mechanisms and the resulting hardness.

Consequently, the lower hardness is likely related to the combined effects of higher Mn content, phase stability, and stacking-fault-energy-controlled deformation behaviour [33]. Upon annealing at 400 °C, the hardness increases by approximately 30%, similar to the $Fe_{1.3}CoNiAl_{1.5}Mn_{2.5}$ alloy, which exhibits a ~50% increase at the same temperature. This enhancement is likely associated with crystal structure reordering and the relaxation of internal stresses. When annealed at 600 °C, the $Fe_{1.1}CoNiAl_{1.5}Mn_{5.4}$ alloy shows a significant decrease of about 85% in hardness, compared with the ~50% reduction observed for the $Fe_{1.3}CoNiAl_{1.5}Mn_{2.5}$ alloy at the same temperature. This pronounced drop is attributed to the formation of a multi-phase structure composed of both BCC and FCC phases, which weakens the overall mechanical strength and may also be associated with oxidation-related changes and stress relaxation during annealing, which together may contribute to the reduced hardness. At 800 °C, the alloy exhibits the presence of FCC metallic and oxide phases, which partially restore the hardness to approximately 6.8 GPa; however, this partial recovery is more likely associated with the FCC metallic phase rather than the oxide phase itself. The $Fe_{1.1}CoNiAl_{1.5}Mn_{5.4}$ samples annealed at 600 °C and 800 °C show remarkable large experimental errors, similar to those observed in the $Fe_{1.3}CoNiAl_{1.5}Mn_{2.5}$ alloy at the same annealing conditions. This behaviour suggests that the surface becomes non-uniform, as indicated by the large data scatter. Such non-uniformity may result from grain coarsening, surface oxidation, and elemental segregation, which collectively produce local variations in composition and hardness. The variations in the reduced modulus and Young's modulus exhibit a trend consistent with that of the hardness, indicating that these properties are governed by similar underlying microstructural mechanisms.

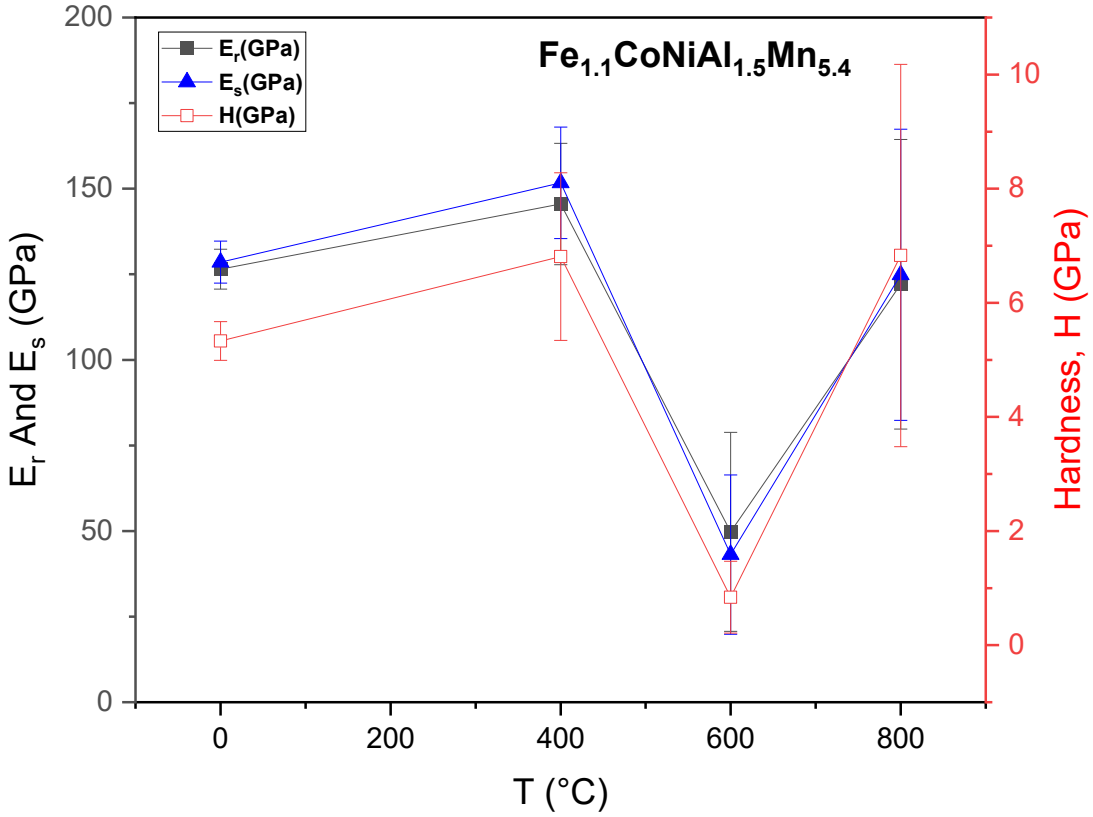

Figure 6. Comparison of hardness (H), Young's modulus (E_s), and reduced modulus (E_r) of $Fe_{1.1}CoNiAl_{1.5}Mn_{5.4}$ alloy at different annealing temperatures. The lines are a guide for the eye.

The yield strength (σ_y) was calculated [39] and plotted for all samples in Figure 7 (a). The as-deposited $FeCoNi_{0.8}$ alloy, along with the $Fe_{1.3}CoNiAl_{1.5}Mn_{2.5}$ and $Fe_{1.1}CoNiAl_{1.5}Mn_{5.4}$ alloy, exhibits very similar values of approximately 900 MPa, with less than 10% variation among the samples. Upon the onset of heat treatment, the variation in yield strength diverges, as the annealing temperature affects each composition differently. For the $FeCoNi_{0.8}$ alloy annealed at 400 °C, the yield strength increases by about 80%, from 910 MPa to 1610 MPa, which correlates with the observed shift of the peak toward higher diffraction angles. However, when the annealing temperature is further increased to 600 °C, the yield strength rises sharply to approximately 6750 MPa. Although this value appears unusually high, it is consistent with Tabor's method [40], which relates the yield strength to the hardness through the empirical correlation $\sigma_y \approx H/3$. Given that the measured hardness is 16 ± 3 GPa, the calculated yield strength is in reasonable agreement with

this relation. The unusually high value observed only for the 600 °C sample may also be influenced by thin-film confinement effects or indentation size effects during nanoindentation.

The $Fe_{1.3}CoNiAl_{1.5}Mn_{2.5}$ alloy exhibits behaviour similar to that of the $FeCoNi_{0.8}$ alloy at both room temperature and after annealing at 400 °C. Upon annealing at 400 °C, the yield strength increases by approximately 70%, which can be attributed to changes in the film morphology, as evidenced by the XRD peak characteristics. In particular, the peak broadening suggests a reduction in grain size, which may contribute to the observed strengthening. At room temperature, the XRD pattern shows a distinct BCC peak; however, after annealing at 400 °C, this peak becomes broader and less intense, suggesting lattice distortion accompanied by a decrease in grain size within the film from approximately 74 Å to 60 Å (calculated using Scherer equation), as well as possible overlapping BCC reflections. When the annealing temperature is raised to 600 °C, the yield strength decreases noticeably, most likely owing to the formation of a dual-phase structure (FCC + BCC), as confirmed by the XRD results. At 800 °C, only minor changes are observed, as the alloy still exhibits a mixed FCC phase composed of both metallic and oxide components.

The $Fe_{1.1}CoNiAl_{1.5}Mn_{5.4}$ alloy shows a similar initial trend, with an increase in yield strength after annealing at 400 °C. However, further annealing at 600 °C results in a sharp decrease to approximately 145 MPa. This substantial drop can be attributed to several factors: the high Mn content, which introduces severe lattice distortion due to its larger atomic radius compared with Fe, Co, and Ni [41]; and the presence of multiple crystalline phases (trigonal, FCC-oxide, FCC-metal, and BCC), which collectively increase brittleness and reduce cohesive strength. Upon annealing at 800 °C, the yield strength partially recovers to a value comparable to that of the $Fe_{1.3}CoNiAl_{1.5}Mn_{2.5}$ alloy at the same temperature, likely due to partial recrystallisation and the stabilisation of the FCC-oxide phase.

Another parameter that can be derived from Figure 3 (a, b, and c) is the elastic recovery of the material. This represents the portion of the film that elastically returns to its original position after the indenter tip is withdrawn. The elastic recovery is quantified as the difference between the maximum indentation depth (h_{max}) and the final indentation depth (h_f) following unloading [34]. Figure 7 (b) illustrates the elastic recovery, which increases with the rise in annealing temperature. However, the $Fe_{1.1}CoNiAl_{1.5}Mn_{5.4}$ alloy at 600 °C does not follow this trend, most likely due to its lower hardness and yield strength values, which can be attributed to the factors mentioned earlier.

Taking account of these findings, the investigated FeCoNi-based alloys demonstrate excellent mechanical stability and tunability through controlled annealing. The ability to optimise hardness, elastic recovery, and yield strength with heat treatment highlights their potential for advanced structural and functional applications. In particular, the balanced combination of strength and ductility observed in the $FeCoNi_{0.8}$ alloy at 600 °C makes it a promising candidate for use in microelectromechanical systems (MEMS), magnetic sensors, and wear-resistant coatings, where high hardness, resistance to deformation, and structural integrity are important [42]. Moreover, the $Fe_{1.1}CoNiAl_{1.5}Mn_{5.4}$ alloy annealed at 600 °C exhibits relatively low hardness (≈0.85 GPa) and

reduced yield strength, which makes it a potential candidate for soft magnetic applications or flexible substrate layers where high ductility, low residual stress, and minimal pinning are advantageous for improving magnetic permeability and mechanical compliance. These properties indicate that the investigated films may be promising for MEMS-related thin-film components and wear-resistant coatings, where resistance to deformation and structural integrity are important [42].

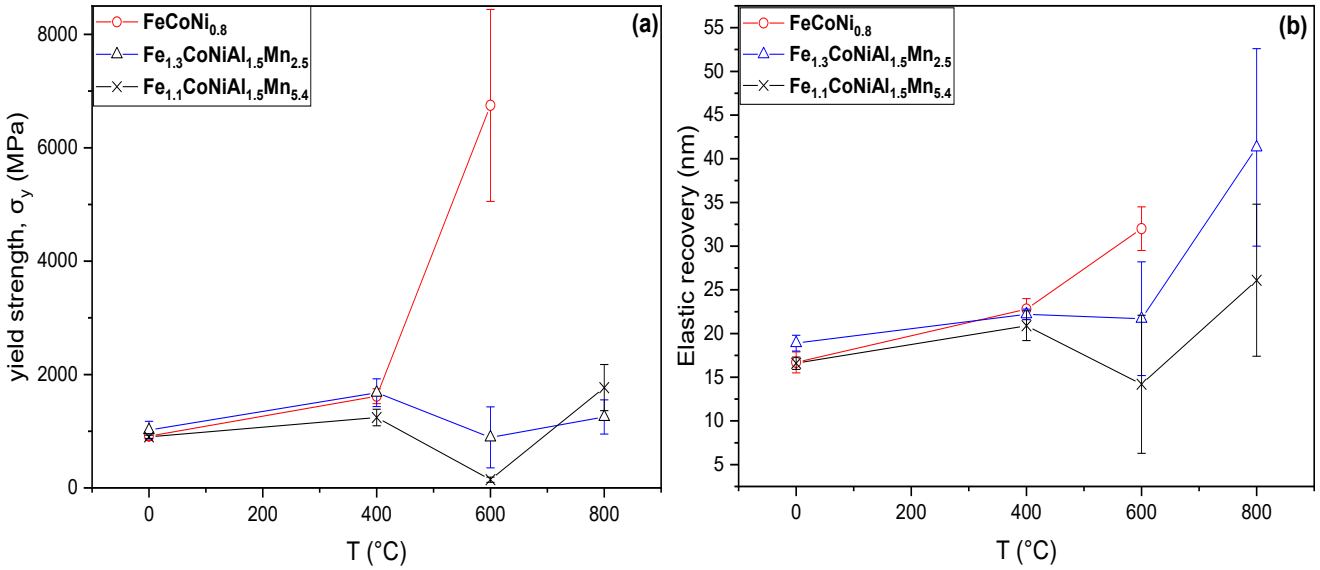

Figure 7. (a) Comparison of yield strength (σ_y), (b) elastic recovery for $FeCoNi_{0.8}$, $Fe_{1.3}CoNiAl_{1.5}Mn_{2.5}$, and $Fe_{1.1}CoNiAl_{1.5}Mn_{5.4}$ alloys as a function of annealing temperature. The lines are a guide for the eye.

Conclusion

In conclusion, FeCoNiAl-based alloys with varying Mn contents were successfully fabricated using DC magnetron sputtering and systematically investigated to elucidate the combined effects of elemental composition and annealing temperature on their structural and mechanical properties. The as-deposited FeCoNi alloy exhibited a predominantly FCC crystal structure, while the incorporation of Al and Mn promoted the formation of a BCC structure, with higher Mn contents leading to weaker and less stable BCC reflections. Upon annealing, pronounced phase transformations were observed, including the formation of FCC oxide phases and the emergence of trigonal Fe_2O_3 in alloys containing Al and Mn at elevated temperatures.

The nanoindentation results demonstrated a strong correlation between phase evolution and mechanical response. The $FeCoNi_{0.8}$ alloy showed a remarkable enhancement in hardness with increasing annealing temperature, reaching a maximum value of approximately 16 GPa at 600 °C, which is attributed to phase transformation and oxide-related strengthening mechanisms. In contrast, alloys containing higher Mn content exhibited reduced hardness and yield strength at elevated temperatures due to multiphase formation, oxidation, and increased brittleness. The evolution of elastic recovery and yield strength further highlighted the sensitivity of mechanical performance to both composition and heat treatment. Overall, these findings provide scientific insight into how composition-dependent phase stability and annealing-induced structural evolution govern the mechanical tuning of sputtered FeCoNi-based thin films, thereby establishing a clear composition–structure–property relationship in these alloy systems.

Acknowledgements

This work was supported by the Henry Royce Institute for Advanced Materials, funded through EPSRC grants EP/R00661X/1, EP/S019367/1, EP/P025021/1 and EP/P025498/1. Also, the authors acknowledge the support of the Government of Saudi Arabia.

References

1. Yeh, J.W., et al., *Nanostructured high-entropy alloys with multiple principal elements: novel alloy design concepts and outcomes*. Advanced engineering materials, 2004. **6**(5): p. 299-303.
2. Cantor, B., et al., *Microstructural development in equiatomic multicomponent alloys*. Materials Science and Engineering: A, 2004. **375**: p. 213-218.
3. Maiti, S. and W. Steurer, *Structural-disorder and its effect on mechanical properties in single-phase TaNbHfZr high-entropy alloy*. Acta Materialia, 2016. **106**: p. 87-97.
4. Gali, A. and E.P. George, *Tensile properties of high-and medium-entropy alloys*. Intermetallics, 2013. **39**: p. 74-78.
5. Zhang, W., P.K. Liaw, and Y. Zhang, *Science and technology in high-entropy alloys*. Science China Materials, 2018. **61**(1): p. 2-22.
6. Li, Z., et al., *Metastable high-entropy dual-phase alloys overcome the strength–ductility trade-off*. Nature, 2016. **534**(7606): p. 227-230.
7. Gludovatz, B., et al., *A fracture-resistant high-entropy alloy for cryogenic applications*. Science, 2014. **345**(6201): p. 1153-1158.
8. Liu, D., J. Cheng, and H. Ling, *Electrochemical behaviours of (NiCoFeCrCu) 95B5 high entropy alloy coatings*. Materials Science and Technology, 2015. **31**(10): p. 1159-1164.
9. Qiu, Y., et al., *Corrosion characteristics of high entropy alloys*. Materials science and technology, 2015. **31**(10): p. 1235-1243.
10. Zou, Y., H. Ma, and R. Spolenak, *Ultrastrong ductile and stable high-entropy alloys at small scales*. Nature communications, 2015. **6**(1): p. 7748.
11. Chen, M.-R., et al., *Effect of vanadium addition on the microstructure, hardness, and wear resistance of Al0. 5CoCrCuFeNi high-entropy alloy*. Metallurgical and Materials Transactions A, 2006. **37**(5): p. 1363-1369.
12. Wang, Y.P., H.Z. Fu, and B.S. Li, *Solid solution or intermetallics in a high-entropy alloy*. Advanced engineering materials, 2009. **11**.
13. Chuang, M.-H., et al., *Microstructure and wear behavior of AlxCo1. 5CrFeNi1. 5Tiy high-entropy alloys*. Acta Materialia, 2011. **59**(16): p. 6308-6317.
14. Alsebaie, D. and N.A. Morley, *Impact of increasing aluminium content on the magnetic, electrical, and structural properties of FeCoNiMnAl thin films*. IEEE Transactions on Magnetics, 2025.
15. Lu, T., et al., *Fine tuning in-sync the mechanical and magnetic properties of FeCoNiAl0. 25Mn0. 25 high-entropy alloy through cold rolling and annealing treatment*. Journal of Materials Processing Technology, 2021. **289**: p. 116945.
16. Duc, L.M., et al. *The Effect of Heat Treatment on Microstructure and Mechanical Properties of FeCoNiAl0. 25Mn0. 75 High Entropy Alloy*. in *Materials Science Forum*. 2024. Trans Tech Publ.
17. Hansen, N., *Hall–Petch relation and boundary strengthening*. Scripta materialia, 2004. **51**(8): p. 801-806.
18. Benjamin, J.S., *Dispersion strengthened superalloys by mechanical alloying*. Metallurgical transactions, 1970. **1**(10): p. 2943-2951.
19. Nagini, M., et al., *Microstructure–mechanical property correlation in oxide dispersion strengthened 18Cr ferritic steel*. Materials Science and Engineering: A, 2017. **708**: p. 451-459.
20. Hadraba, H., et al., *Oxide dispersion strengthened CoCrFeNiMn high-entropy alloy*. Materials Science and Engineering: A, 2017. **689**: p. 252-256.
21. Du, X., et al., *Enhance the mechanical properties of CoCrFeNi high entropy alloy: Rare-earth element Gd was employed as a "cladding structure" to refine grains*. Materials Today Communications, 2024. **41**: p. 110732.
22. Tekin, M., et al., *Unveiling the creep mechanisms of rare earth element yttrium added and SPS consolidated CoCrFeNi high entropy alloys*. Materials Testing, 2025. **67**(9): p. 1495-1506.
23. Tekin, M., et al., *Microstructural evolution, nanoindentation creep response, and wear properties of Y2O3-modified CoCrFeNi high entropy alloys*. Materials Characterization, 2026. **231**: p. 115942.
24. Lin, C.-M. and H.-L. Tsai, *Evolution of microstructure, hardness, and corrosion properties of high-entropy Al0. 5CoCrFeNi alloy*. Intermetallics, 2011. **19**(3): p. 288-294.
25. Li, L.-Z., et al., *Effects of annealing temperature on the structure and static magnetic properties of NiZnCo ferrite thin films*. Journal of Magnetism and Magnetic Materials, 2014. **368**: p. 8-11.
26. Belmeguenai, M., et al., *Annealing temperature and thickness dependencies of structural and magnetic properties of Co 2 FeAl thin films*. Phys. Rev. B, 2016. **94**(104424): p. 10.1103.
27. Alsebaie, D.M. and N. Morley, *Structural and magnetic evolution of FeCoNiAlMn thin films under varying Mn content and annealing temperatures*. Journal of King Saud University–Science, 2026.
28. Guo, S., et al., *Effect of valence electron concentration on stability of fcc or bcc phase in high entropy alloys*. Journal of applied physics, 2011. **109**(10).

29. Yang, Y.-C., et al., *Low-resistivity oxides in Ti x FeCoNi thin films after vacuum annealing*. Surface engineering, 2018. **34**(9): p. 667-673.
30. Bazioti, C., et al., *Probing the structural evolution and its impact on magnetic properties of FeCoNi (AlMn) x high-entropy alloy at the nanoscale*. Journal of Alloys and Compounds, 2022. **910**: p. 164724.
31. Rowan-Robinson, R.M., Z. Leong, and N.A. Morley, *CoFeMn0.5Al0.25: A high magnetisation CoFe based soft alloy with reduced Co content*. Materials Chemistry and Physics, 2023. **299**: p. 127518.
32. Morley, N.A., et al., *Magnetic properties of the complex concentrated alloy system CoFeNi0.5Cr0.5Alx*. Scientific Reports, 2020. **10**(1): p. 14506.
33. Emsley, J., *Nature's building blocks: an AZ guide to the elements*. 2011: Oxford University Press.
34. Abbas, Q.A., et al., *Comparison of the mechanical properties of amorphous FeSiB and FeGaSiB films*. Materials Research Express, 2025. **12**(9): p. 096403.
35. Oliver, W.C. and G.M. Pharr, *An improved technique for determining hardness and elastic modulus using load and displacement sensing indentation experiments*. Journal of materials research, 1992. **7**(6): p. 1564-1583.
36. Oliver, W.C. and G.M. Pharr, *Measurement of hardness and elastic modulus by instrumented indentation: Advances in understanding and refinements to methodology*. Journal of materials research, 2004. **19**(1): p. 3-20.
37. Alaneme, K.K., et al., *Nanoindentation studies and analysis of the mechanical properties of Ti-Nb2O5 based composites*. Manufacturing Review, 2020. **7**: p. 19.
38. Baco, S., et al., *An investigation on the mechanical properties of soft magnetostrictive FeCoCr films by nanoindentation*. Journal of alloys and compounds, 2021. **881**: p. 160549.
39. Giannakopoulos, A. and S. Suresh, *Determination of elastoplastic properties by instrumented sharp indentation*. Scripta materialia, 1999. **40**(10): p. 1191-1198.
40. Cahoon, J., W. Broughton, and A. Kutzak, *The determination of yield strength from hardness measurements*. Metallurgical transactions, 1971. **2**(7): p. 1979-1983.
41. Akbari, A., et al., *Effects of annealing and cold rolling on microstructural features, magnetic properties, tensile behavior and electrical resistance of FeCoNi(MnAl)x high entropy alloys*. Intermetallics, 2024. **175**: p. 108521.
42. Ando, T. and X.-A. Fu, *Materials: Silicon and beyond*. Sensors and Actuators A: Physical, 2019. **296**: p. 340-351.